

## Dynamical Impact of <sup>56</sup>Ni Heating in the Pair-Instability Supernovae

KE-JUNG CHEN<sup>1</sup> AND S. E. WOOSLEY<sup>2</sup>

<sup>1</sup>*Institute of Astronomy and Astrophysics, Academia Sinica, Taipei 10617, Taiwan*

<sup>2</sup>*Department of Astronomy and Astrophysics, University of California at Santa Cruz, Santa Cruz, CA 95060, USA*

### ABSTRACT

We examine the radioactivity heating of <sup>56</sup>Ni decay in the pair-instability supernovae with two-dimensional simulations. Pair-instability supernovae form from the death of very massive stars of 140–260  $M_{\odot}$ . Their explosions are triggered by the contract of the core due to the electron-positron pair production instability, which ignites the explosive burning of oxygen and silicon and eventually blows up the entire star without leaving any compact remnants. Depending on the mass of the progenitor star, about 0.1–30  $M_{\odot}$  of radioactive isotope, <sup>56</sup>Ni can be synthesized during the explosion. If the amount of <sup>56</sup>Ni exceeds 5  $M_{\odot}$ , the decay energy of <sup>56</sup>Ni may power a luminous transit by providing  $\sim 10^{51}$  erg of radiation energy. However, such a large energy injection likely not only produces radiation but also changes the dynamics of the ejecta. We investigate the effect of <sup>56</sup>Ni radioactive heating by performing high-resolution two-dimensional simulations and find the <sup>56</sup>Ni heating creates a shell in the inner boundary of a silicon burning shell about 200 days after the explosion. However, it does not dredge up the <sup>56</sup>Ni to further mix with the outer layers of <sup>16</sup>O or beyond. In addition, this shell distorts the inner ejecta without breaking down its spherical symmetry. Therefore, <sup>56</sup>Ni heating to the dynamics of ejecta is not strong enough to alter the change of PISNe spectra through mixing. Nevertheless, the PISNe light curve becomes dimmer because part of the radioactive energy is used to push out the ejecta instead of turning into radiation.

*Keywords:* Pair-instability supernovae – <sup>56</sup>Ni decay – Shock wave – Fluid instabilities

### 1. INTRODUCTION

Very Massive Stars (VMS) of 140–260  $M_{\odot}$  are thought to die as pair-instability supernovae (Woosley et al. 2002). The original idea of pair-instability was introduced by Barkat et al. (1967), further developed by Ober et al. (1983); Glatzel et al. (1985); Stringfellow & Woosley (1988); Heger & Woosley (2002, 2010). When the core of VMS evolves to a temperature of  $> 10^9$  K,

energetic photons ( $h\nu \geq 1\text{Mev}$ ) in the tail of Maxwellian distribution start to convert into electron ( $e^-$ ) and positron ( $e^+$ ) pairs through photons and nuclei collisions. The pair-production removes the central radiation pressure then triggers a dramatic contraction of the core. The rising temperature and density eventually ignite the explosive oxygen and silicon burning that completely disrupts the entire star. It is called a pair-instability supernova (PISN), producing  $10^{52} - 10^{53}$  erg of explosion energy and 0.1–30  $M_{\odot}$  of <sup>56</sup>Ni, and is thought to be the biggest thermonuclear explosions in the universe. The physics of thermonuclear ex-

plosions are better understood; therefore, the explosion mechanics of PISNe are more robust than those of the core-collapse SNe. A large amount of  $^{56}\text{Ni}$  makes PISNe luminous transits for probing the universe.

Recently, [Chatzopoulos et al. \(2015\)](#) suggested that the rotation can shift the lower mass limit of the progenitor stars from 140 to 85  $M_{\odot}$ , and [Chen \(2015\)](#) found that  $^{56}\text{Ni}$  production decreases significantly in the rapidly rotating PISNe. More sophisticated multidimensional models of PISNe had been recently done by [Chen et al. \(2011, 2014\)](#) and [Gilmer et al. \(2017\)](#). Observations by [Humphreys & Davidson \(1979\)](#); [Davidson & Humphreys \(1997\)](#); [Crowther et al. \(2010\)](#) suggested the formation of VMS  $> 100M_{\odot}$  in our galactic center. Recent cosmological simulations ([Hirano et al. 2014](#)) also suggested that, given the top-heavy initial mass function (IMF) for Pop III stars, many of the first stars would have died as PISNe. These results suggest that PISNe may occur in both the local and early universe.

Observational signatures predicted by [Kasen et al. \(2011\)](#), [Kozyreva et al. \(2014\)](#), [Kozyreva & Blinnikov \(2015\)](#), and [Whalen et al. \(2014\)](#) suggest that PISNe will be visible in the near-infrared (NIR) at  $z \sim 10-15$  to the *James Webb Space Telescope (JWST)*, the *Wide-Field Infrared Survey Telescope (WFIRST)*, and the next generation of extremely large telescopes. Therefore, PISNe could probe the masses of the first generation of stars (see also [Hummel et al. 2012](#); [Chatzopoulos & Wheeler 2012](#); [Pan et al. 2012](#); [Whalen et al. 2013](#); [Meiksin & Whalen 2013](#); [de Souza et al. 2013](#); [Mesler et al. 2014](#)) and probe the extreme metal pool stars, such as [Hartwig et al. \(2018\)](#); [Takahashi et al. \(2018\)](#).

[Kasen et al. \(2011\)](#) presented detailed light curves and spectra from the 1D PISNe models of [Heger & Woosley \(2010\)](#). The energy from PISN was mainly powered by the decay energy of  $^{56}\text{Ni}$ , which first releases in the form  $\gamma$ -ray, then, reprocessed by the inner ejecta, eventually emerges as

UV/optical. In the current models of synthesized light curves and spectra, nearly 100%  $^{56}\text{Ni}$  decay energy is assumed to turn into radiation.

The total amount of decay energy of  $5 M_{\odot} ^{56}\text{Ni}$  is  $\sim 1 \times 10^{51}$  erg; that is comparable to an explosion energy of a collapsed SN. Such an energy deposited on the PISN ejecta may change its dynamics: the  $^{56}\text{Ni}$  heating can push up gas and drive fluid instabilities. This is called the Ni bubble issue, and it has been seen in the previous 1D radiation transfer calculations by [Whalen et al. \(2014\)](#) and [Kozyreva & Blinnikov \(2015\)](#). However, so far no literature addresses this issue in detail. Current multidimensional models generated by [Chen et al. \(2011, 2014\)](#) and [Gilmer et al. \(2017\)](#) have not run their simulations long enough ( $> 100$  days) to examine the dynamical effect of  $^{56}\text{Ni}$  heating. To resolve this issue, we use high-resolution 2D simulations of PISNe to investigate the  $^{56}\text{Ni}$  heating issue. The goals of this paper are to evaluate the dynamics or mixing of ejecta due to  $^{56}\text{Ni}$  heating and discuss how they affect the light curves/spectra of PISNe.

The structure of the paper is as follows: we first describe the numerical approaches in Section 2. Then we present our results in Section 3. We discuss the physical implications of the results in Section 4 and conclude in Section 5.

## 2. NUMERICAL APPROACHES

### 2.1. Progenitor Stars

We select three representative PISN models that produce  $\sim 5-20 M_{\odot} ^{56}\text{Ni}$  from different progenitor stars, including two helium stars and one red supergiant in this work. For VMS of non-zero metallicity, their surface luminosity is close to Eddington and drives strong stellar winds to strip out the outer envelopes. However, the mass-loss mechanics are poorly understood. Therefore, we evolved two helium stars of 105  $M_{\odot}$  and 110  $M_{\odot}$  with the stellar evolution code, KEPLER ([Weaver et al. 1978](#); [Heger & Woosley 2010](#)). The helium stars mimic the helium core of VMS; the result pro-

vides a better mass indicator to determine the fates of massive stars. We select two helium stars of 105 (He105) and 110 (He110)  $M_{\odot}$ , which eventually die as PISNe with 8.53 and 13.13  $M_{\odot}$  of  $^{56}\text{Ni}$ , respectively. To compare with an unstrapped-envelope progenitor, we select a 225 (U225)  $M_{\odot}$  star of 0.1  $Z_{\odot}$ , which evolves to a red supergiant of an extensive hydrogen envelope that inflates the original radius of the star to 100 times larger. During the post-main sequence, the carbon and oxygen in the central convection core are getting closer to the hydrogen-burning shell. When any convective overshoot or other convective boundary mixing (Meakin & Arnett 2007; Arnett et al. 2009; Woodward et al. 2014) occurs, the star evolves into a red super giant. This 225  $M_{\odot}$  star eventually dies as a PISN and produces 16.52  $M_{\odot}$  of  $^{56}\text{Ni}$ . The physical properties of three progenitor stars and their PISNe are listed in Table 1.

PISNe are driven mainly by the thermonuclear explosions of  $^{16}\text{O}$  and  $^{28}\text{Si}$  burning, and the underlying physics is well understood. Therefore, PISNe can be blown up in 1D KEPLER self-consistently. The three 1D PISN progenitor models ran until all nuclear burning was finished, so no more energy and isotopes would change. At this time, the forward shock of explosions in He105 and He110 has just broken out of the stellar surface. Instead, the shock in U225 has just entered its hydrogen envelope. Chen et al. (2014) simulated PISNe from the onset of core contraction to explosions. Their results suggested that the initial explosions produce only minor fluid instabilities driven by explosive burning in the post-shock region within a short time scale of  $\sim 100$  sec. Given the amplitude and scale of this mixing, it is tiny compared to the overall structures of ejecta. Also, the fluid instabilities during the core contraction and bounce are much weaker than those found in the core-collapse SNe. Therefore, the mixing during the explosive burning phase can be treated as perturbations in the 2D simulations here.

Fig. 1 shows the chemical abundance pattern of the three models when they were mapped onto the 2D CASTRO simulations. The abundance patterns show distinctive layers of different elements. None of the  $^{56}\text{Ni}$  is mixed with the  $^{16}\text{O}$  and  $^{12}\text{C}$  layers. Fig. 2 shows the corresponding density and velocity of Fig. 1. The forward shock velocity of He105 and He110 is  $\sim 2 \times 10^9$  cm sec $^{-1}$ . Because the entire helium star becomes unbound, its central densities drop to  $\sim 200$  g cm $^{-3}$ . For the U225 model, the shock still propagates within the hydrogen envelope, and its velocity is  $\sim 2 \times 10^9$  cm sec $^{-1}$ . Its central density is  $\sim 1$  g cm $^{-3}$ . There is no sight of reverse shock or any fluid instabilities in the three progenitor stars. Therefore, if any mixing occurs later, it must be caused by the shock propagation or by  $^{56}\text{Ni}$  decay heating it. These 1D KEPLER results are also supported by the 2D PISN simulations from (Chen et al. 2011), which carried high-resolution simulations to examine the fluid instabilities during the initial core contraction and bounce phase. Only mild mixing is driven by the burning of  $^4\text{He}$  behind the shock in the oxygen burning shell. Due to a short burning time of tens of sec, fluid instabilities cannot grow significantly. Therefore, we seed  $\sim 3\%$  of density fluctuations into 2D simulations by considering the initial fluid instabilities before the shock launched.

## 2.2. 2D CASTRO Setup

We carry out 2D simulations with CASTRO, a multidimensional adaptive mesh refinement (AMR) hydrodynamics code for astrophysical simulations (Almgren et al. 2010; Zhang et al. 2011). The hydro scheme in CASTRO uses an unsplit piecewise parabolic method (PPM) (Colella & Woodward 1984) supported with multispecies advection, and it allows various types of equations of state (EOS). The KEPLER PISN models of densities, velocities, temperatures, and elemental abundances are directly mapped onto 2D cylindrical AMR grids of CASTRO. We use the mapping scheme developed by Chen et al. (2013) to map the 1D physical quantities such as mass, momen-

**Table 1.** Progenitor Models

Model	Stellar mass ( $M_{\odot}$ )	Stellar radius ( $10^{12}$ cm)	He core mass ( $M_{\odot}$ )	Explosion energy Bethe ( $10^{51}$ erg)	$^{56}\text{Ni}$ production ( $M_{\odot}$ )	Radioactive energy Bethe ( $10^{51}$ erg)
He105	105	1.42	105	48.3	8.53	1.58
He110	110	1.43	110	55.3	13.13	2.47
U225	225	334	104	46.6	16.52	3.07

NOTE—Radioactive energy of  $1 M_{\odot} \text{ } ^{56}\text{Ni} \rightarrow \text{}^{56}\text{Co} \rightarrow \text{}^{56}\text{Fe}$  decay is  $\sim 1.86 \times 10^{50}$  erg.

tum, and energy onto multidimensional grids of CASTRO conservatively.

To investigate how mixing impacts the evolution of abundance pattern of yields, we follow the evolution of thirteen species that constitute the PISNe ejecta:  $^1\text{H}$ ,  $^4\text{He}$ ,  $^{12}\text{C}$ ,  $^{16}\text{O}$ ,  $^{20}\text{Ne}$ ,  $^{24}\text{Mg}$ ,  $^{28}\text{Si}$ ,  $^{36}\text{Ar}$ ,  $^{40}\text{Ca}$ ,  $^{44}\text{Ti}$ ,  $^{48}\text{Cr}$ ,  $^{56}\text{Fe}$ , and  $^{56}\text{Ni}$ . The simulations adopt the Helmholtz EOS (Timmes & Swesty 2000), including contributions by both degenerate and non-degenerate relativistic and non-relativistic electrons, electron-positron pairs, ions, and radiation, during the early phase of explosion, and switch to the ideal gas EOS later, for the gas density becomes  $< 10^{-12} \text{g cm}^{-3}$ . The gravity solver uses the monopole approximation by constructing a spherically symmetric gravitational potential from the radial average of the density and then calculating the corresponding gravitational force for everywhere in the AMR hierarchy. It is a well-suited approximation to the matter distribution of the supernovae in which global spherical structure is a reasonable assumption.

We simulate only an octant star in 2D. The physical size of the domain in  $r$  and  $z$  is  $\sim 1.2 \times 10^{16}$  cm, which is  $\sim 10,000$  and 100 times larger than the radius of the helium star and red supergiant, respectively. The large size of the domain allows us to follow the shock and dynamics of ejecta for a long time ( $> 300$  days since the explosion). Because hydro simulations are not allowed to take zero/negative density in the grid, it is necessary to fill the gas outside the 1D stellar profile

from KEPLER. The circumstellar medium (CSM) of VMS (depending on their radiation, mass-loss history, stellar wind, and environmental ISM) is subject to great uncertainties. To address this issue, we fill the CSM with an ambient gas of density profile,  $\rho = 10^{-4} \rho_s (\frac{r}{r_s})^{-2}$ ;  $\rho_s$  and  $r_s$  is the surface density and radius of the star. The total mass of this artificial medium for the He105/He110 is  $\sim 4 \times 10^{-5} M_{\odot}$ , and for U225 it is  $\sim 0.05 M_{\odot}$  for the entire simulation domain. This density profile of  $\rho \propto r^{-2}$  is physically motivated by the stellar wind from the mass loss of massive stars, and it also prevents artificial mixing caused by the reverse shock when the forward shock runs into this CSM.

The base grid of our 2D setup has  $256 \times 256$  zones, with eight levels of AMR for an additional factor of up to 256 ( $2^8$ ) in the spacial resolution. The grid refinement criteria are based on gradients of gas density, velocity, and pressure. The hierarchy nested grids are also constructed in such a way that the  $^{56}\text{Ni}$ -rich region always receives the highest resolution. The simulation box uses reflect and outflow boundary conditions on the inner and outer boundaries in both  $r$  and  $z$ , respectively. Since we simulate a huge domain, to maintain the high resolution as the simulation is evolving, we use the *Embiggen* approach by gradually expanding the simulation box as the shock evolves (Chen et al. 2013), which effectively applies for the optimal resolution to follow the fluid instabilities to a large scale. We use three times *Embiggen* of a factor of four and results in the overall effective resolution of  $2^{22} \times 2^{22}$

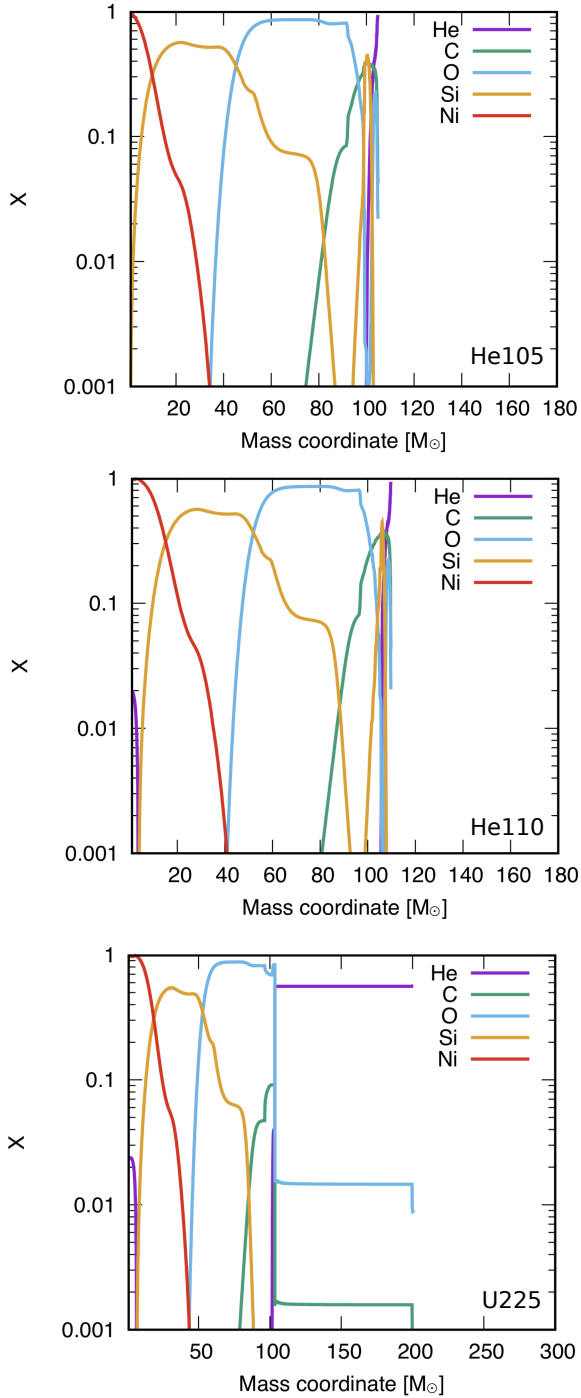


**Figure 1.** Initial chemical abundance patterns of the He105, He110, and U225 models. These patterns show the onion-like structure of chemical compositions because there is no mixing between different burning shells in the 1D stellar model. The He105 and He110 models are helium stars, so they do not have an extensive hydrogen envelope like that of the full star model, U225.

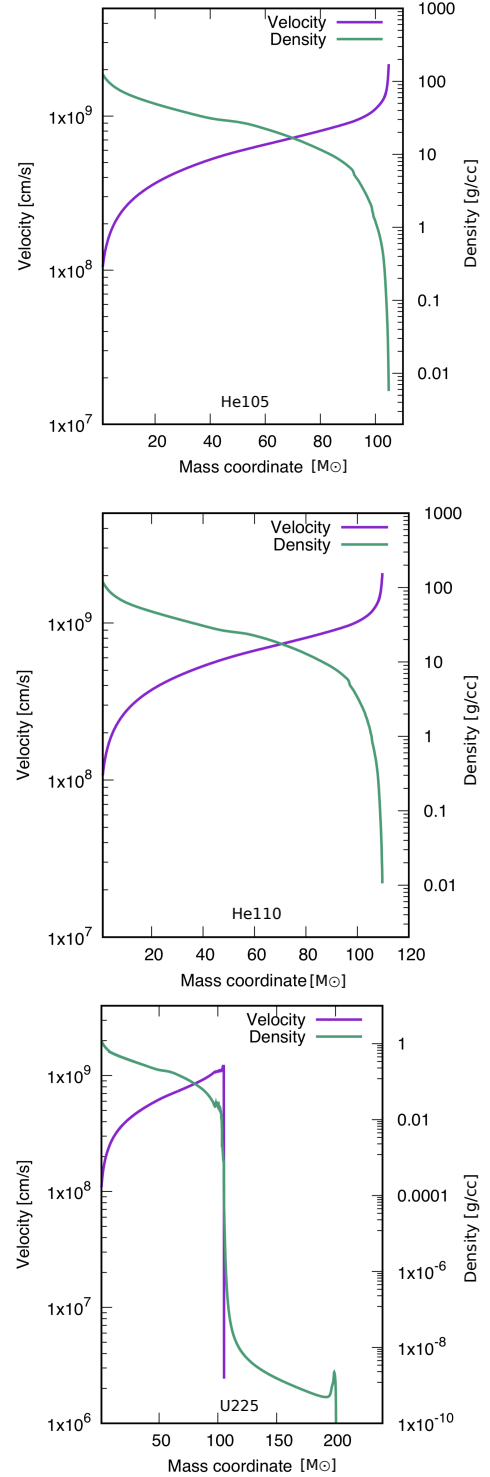


**Figure 2.** Initial velocity and density of He105, He110, and U225 models. The forward shock from the explosion has just broken the stellar surface in the He105 and He110 models. At the same time, the shock in U225 has just entered its hydrogen envelope.

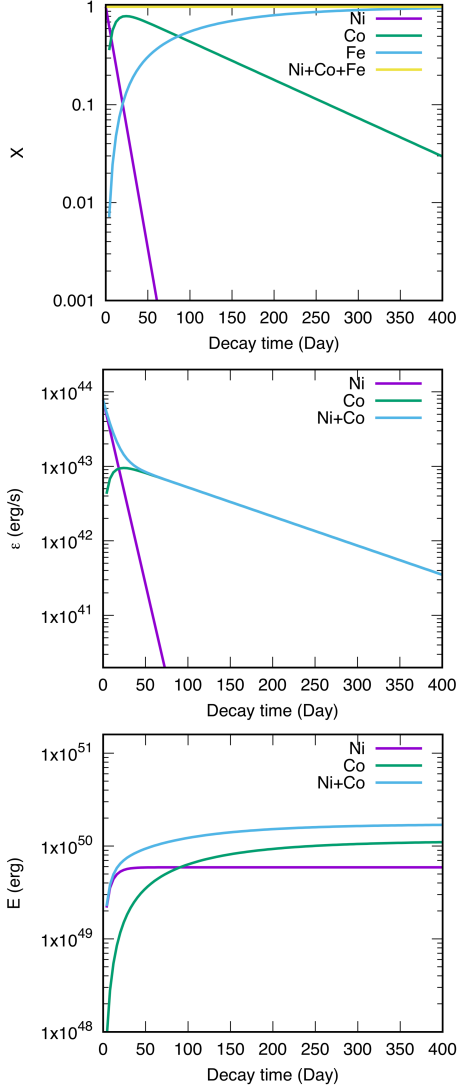


**Figure 3.** Decay of  $1 M_{\odot}$   $^{56}\text{Ni}$ . The upper panel (the evolution mass fraction of  $^{56}\text{Ni}$ ,  $^{56}\text{Co}$ , and  $^{56}\text{Fe}$ ):  $\sim 90\%$  of  $^{56}\text{Ni}$  decays into  $^{56}\text{Co}$  within the first 20 days, then  $^{56}\text{Co}$  again decays into a stable isotope,  $^{56}\text{Fe}$ , within 250 days. The middle panel (energy generation rates of  $^{56}\text{Ni}$ , and  $^{56}\text{Co}$  decay): In the first 50 days, the energy generation rates can reach as high as  $10^{43}$  erg  $\text{sec}^{-1}$ . If all of this energy turns into radiation, then it can provide a luminous transit. The late-time ( $> 50$  days) energy input is dominated by  $^{56}\text{Co}$  decay, which is thought to power the SN light curve. The bottom panel (total energy): The total amount of energy available from  $^{56}\text{Ni} \rightarrow ^{56}\text{Co}$  decay is  $\sim 5.92 \times 10^{49}$  erg, and for  $^{56}\text{Co} \rightarrow ^{56}\text{Fe}$  is  $\sim 1.28 \times 10^{50}$  erg. Therefore,  $^{56}\text{Ni} \rightarrow ^{56}\text{Co} \rightarrow ^{56}\text{Fe}$  decay releases  $\sim 1.8 \times 10^{50}$  erg within 250 days.

to resolve  $10^{16} \times 10^{16}$   $\text{cm}^2$ . The finest spacial resolution achieves  $\sim 2.38 \times 10^9$  cm, while the radius is  $\sim 3.34 \times 10^{14}$  cm for the U225 model and  $1.43 \times 10^{12}$  cm for both the He105/He110 models. Chen et al. (2014) did careful resolution studies of multidimensional simulations of PISNe. Their results suggested that resolving the pure-hydro instabilities without a nuclear burning requires  $\sim 5 \times 10^9$  cm when the fluid instabilities start to appear. Therefore, the resolution applied here is sufficient to catch the features of emergent fluid instabilities and follow the later mixing.

### 2.3. Radioactive Energy of $^{56}\text{Ni}$ Decay

The radioactive isotope  $^{56}\text{Ni}$  is made through explosive silicon burning. It first decays  $\rightarrow ^{56}\text{Co}$ ,  $\rightarrow ^{56}\text{Fe}$ . The half-life time of  $^{56}\text{Ni}$  is  $\sim 6.1$  days and of  $^{56}\text{Co}$  is  $\sim 77.1$  days. The energy released from this decay chain is the main energy source to power most of the SNe light curves. A physical module is included in CASTRO to couple the decay energy of  $^{56}\text{Ni}$  with the gas dynamics. The energy generation rate  $\dot{\epsilon}_{56\text{Ni}}$  (erg  $\text{cm}^{-3}$   $\text{sec}^{-1}$ ) from the  $^{56}\text{Ni}$  to  $^{56}\text{Co}$  decay per unit volume can be expressed as:

$$\dot{\epsilon}_{56\text{Ni}}(t) = \lambda_{56\text{Ni}} \rho X_{56\text{Ni}} Q_{56\text{Ni}} e^{-\lambda_{56\text{Ni}} t}, \quad (1)$$

where  $X_{56\text{Ni}}$  is the mass fraction of  $^{56}\text{Ni}$  and  $\rho$  the gas density ( $\text{g cm}^{-3}$ ). The decay rate of  $^{56}\text{Ni}$ ,  $\lambda_{56\text{Ni}}$ , is  $1.315 \times 10^{-6}$   $\text{sec}^{-1}$ , and the amount of energy released per gram of decaying  $^{56}\text{Ni}$  is  $Q_{56\text{Ni}}$  is  $\sim 2.96 \times 10^{16}$  erg  $\text{g}^{-1}$  based on the data from Nadyozhin (1994). The amount of  $^{56}\text{Co}$  at a given time could be found as a function of the amount of initial  $^{56}\text{Ni}$  by

$$X_{56\text{Co}}(t) = \frac{\lambda_{56\text{Ni}}}{\lambda_{56\text{Ni}} - \lambda_{56\text{Co}}} X_{56\text{Ni}} (e^{-\lambda_{56\text{Co}} t} - e^{-\lambda_{56\text{Ni}} t}), \quad (2)$$

so that the energy generation rate  $\dot{\epsilon}_{56\text{Co}}$  (erg  $\text{cm}^{-3}$   $\text{sec}^{-1}$ ) from  $^{56}\text{Co}$  to  $^{56}\text{Fe}$  as a function of time is given by

$$\dot{\epsilon}_{56\text{Co}}(t) = \frac{\lambda_{56\text{Co}} \lambda_{56\text{Ni}}}{\lambda_{56\text{Ni}} - \lambda_{56\text{Co}}} \rho X_{56\text{Ni}} Q_{56\text{Co}} (e^{-\lambda_{56\text{Co}} t} - e^{-\lambda_{56\text{Ni}} t}), \quad (3)$$

with a decay rate for  $^{56}\text{Co}$ ,  $\lambda_{^{56}\text{Co}}$ , of  $1.042 \times 10^{-7} \text{ sec}^{-1}$ , and an energy per gram of decaying  $^{56}\text{Co}$ ,  $Q_{^{56}\text{Co}}$  is  $\sim 6.4 \times 10^{16} \text{ erg g}^{-1}$  (Nadyozhin 1994). The energy released from the above decay is in the form of  $\gamma$ -ray, which is immediately absorbed by the surrounding dense gas, then it reprocesses the  $\gamma$ -ray to the thermal energy of gas. Therefore, we assume all the decay energy is deposited onto the internal energy of the gas in the simulations. This assumption is valid when the  $^{56}\text{Ni}$  is not yet exposed to the optically thin region within  $\sim 250$  days (assuming three e-folding time of  $^{56}\text{Co}$ ) since the explosion.

To better understand the physics behind the  $^{56}\text{Ni}$  decay, we plot the evolution of mass fraction, energy release rates, and the total energy of one  $M_{\odot}$   $^{56}\text{Ni}$  decay in Fig. 3. A total amount of  $1.8 \times 10^{50}$  ( $\sim 5.92 \times 10^{49}$  from  $^{56}\text{Ni} \rightarrow ^{56}\text{Co}$ ,  $\sim 1.28 \times 10^{50}$  from  $^{56}\text{Co} \rightarrow ^{56}\text{Fe}$ ) erg releases from the decay of one solar mass of  $^{56}\text{Ni}$  in  $\sim 250$  days. Assuming the total amount of decay energy converts into the radiation at the later time (100 days since explosion), it requires about  $\geq 5 M_{\odot}$   $^{56}\text{Ni}$  to make the PISN become a superluminous supernovae (SLSN), which has a budget of radiation energy of  $10^{51}$  erg. It requires the progenitor star to have a mass of  $\geq 200 M_{\odot}$ .

The energy from  $^{56}\text{Ni}$  decay chain is thought to be the primary source for powering the luminous light curves of PISNe. However, it is unclear what fraction of decay energy turns into radiation and what fraction to the dynamical work. Since  $^{56}\text{Ni}$  is made at the stellar center, where the explosion occurs, this decay energy injection from the center is likely to affect the dynamics ejecta and possibly drive fluid instabilities to mix its yields. Such an inside-out mixing could change the observational signatures of PISNe.

### 3. DYNAMICS OF PISNE EJECTA

The explosive oxygen and silicon burning generates about  $\sim 4.8 - 5.5 \times 10^{52}$  erg explosion energy in He105/He110/U225 models and has successfully launched a strong shock that disrupts the

entire star without leaving any compact objects. We follow the forward shock and the expanding ejecta for  $\sim 300$  days until most of the  $^{56}\text{Ni}$  decay energy has been released. Fig. 4 shows the evolution of gas density and  $^{56}\text{Ni}$  mass fraction from our simulations at 20, 100, and 300 days after the explosion. Since we do not specifically trace the advection of  $^{56}\text{Co}$  and  $^{56}\text{Fe}$ ,  $^{56}\text{Ni}$  at the later time refers to the combined isotopes of  $^{56}\text{Ni} + ^{56}\text{Co} + ^{56}\text{Fe}$  and the individual mass fraction can be obtained from Fig. 3.

Due to a short half-life time of  $^{56}\text{Ni} \rightarrow ^{56}\text{Co} \sim 6.1$  days, most of the energy from  $^{56}\text{Ni} \rightarrow ^{56}\text{Co}$  decay has released at 20 days. Rayleigh-Taylor (RT) fingers emerge behind the forward shock in He105 and He110 models. They are caused by the reflective wave when the shock exits the stellar surface. The  $^{56}\text{Ni}$ -rich region still remains at the inner ejecta and far away from the RT fingers. Therefore,  $^{56}\text{Ni}$  distribution is not affected by this early mixing. However, at the same time, more extensive mixing appears in U22; the RT fingers approach the edge of its  $^{56}\text{Ni}$ -rich core. The mixing in U225 is mainly driven by a reverse shock. When the forward shock enters the extensive hydrogen envelope, the shock is slowed down, and the deceleration of sonic waves then forms into a reverse shock. Since the density of ejecta is decreasing outward, the reverse shock provides pressure inversion opposite to its density gradient. The contact discontinuity of ejecta is now subject to RT instabilities when it fulfills the following conditions:

$$\frac{\partial \rho}{\partial r} \frac{\partial P}{\partial r} < 0, \quad (4)$$

where  $\rho$  is the gas density, and  $P$  is the gas pressure. The same RT mixing is frequently found in the PISNe of red supergiant progenitor stars (Chen et al. 2014). There is no sight of mixing driven by  $^{56}\text{Ni}$  decay heating from the most inner ejecta among three models at 20 days since the explosion. The only mixing comes from the forward shock propagation.

$^{56}\text{Co} \rightarrow ^{56}\text{Fe}$  becomes the dominating channel of energy source 60 days after the explosion. Mixing in U225 continues growth and starts to affect its  $^{56}\text{Ni}$ . However, there is no visible mixing in He105 and He110. At 300 days, the  $^{56}\text{Ni}$ -rich region has expanded to the size of  $r \sim 10^{16}$  cm, and more than 95% of the decay has been deposited in the gas. The radioactive energy heats the gas ahead of it and piles them up into a shell. The thickness of the shell is  $\delta r \sim 10^{15}$  cm at 300 days, and it remains marginally in spherical symmetry in He105 and He110, but it is heavily distorted in U225.

Fig. 5 compares the 2D elemental mixing between the He110 and U225 model at the different times. In addition, a trace amount of mixing of  $^{12}\text{C}$  appears at the outer layer; the distribution of elements ( $^{16}\text{O}$ ,  $^{28}\text{Si}$ , ...,  $^{56}\text{Ni}$ ) remains onion-like in He110. However, more extensive mixing of elements can be found in the U225 model, which shows the strong mixture of shells of  $^{12}\text{C}$ ,  $^{16}\text{O}$ ,  $^{28}\text{Si}$ , with part of the central  $^{56}\text{Ni}$ .

#### 4. DYNAMICAL EFFECT OF $^{56}\text{Ni}$ HEATING

We evaluate the mixing of SN ejecta by comparing the spacial distribution of chemical elements (we refer to this as an abundance pattern) at different times. To better quantify the amount of mixing, we plot the 1D angle-averaged abundance patterns at 20 and 200 days since the explosion in Fig. 6. Although the amount of  $^{56}\text{Ni}$  mass in He105 and He110 differs by  $5 M_{\odot}$ , their abundance patterns look pretty similar to each other and remain unchanged with time. Each burning layer stays intact after the explosions, which suggests that the mixing is weak. On the contrary, U225 shows wiggly patterns of  $^{12}\text{C}$ ,  $^{16}\text{O}$ , and  $^{28}\text{Si}$ ; those were dragged to the outer edge of the  $^{56}\text{Ni}$  core region. The velocities of the forward shocks in this model are about  $2 \times 10^9$  cm sec $^{-1}$ . At 200 days since explosion, the forward shock has propagated above  $r \sim 1.2 \times 10^{16}$  cm,  $\sim 90\%$  of radioactive energy is released, and mixing starts to freeze. The boundary between  $X_{^{56}\text{Ni}}$  and  $X_{^{16}\text{O}}$  layers remains at  $10^{-2}$ , suggesting scant dredging up of  $^{56}\text{Ni}$  in the He105

and He110 model.  $^{56}\text{Ni}$  mixed with  $^{16}\text{O}$  and  $^{12}\text{C}$  in the  $r \sim 6-8 \times 10^{15}$  cm is found in U225. Fig. 7 shows the angle-averaged density profiles of the three models. The density bumps are located at  $r \sim 4-6 \times 10^{15}$  cm and have a width of  $\Delta r \sim 10^{15}$  cm. Its density constraint is about 3-4 times higher than its surrounding. It is unlikely that the density bump can evolve further without additional energy inputs. Therefore, our results suggest  $^{56}\text{Ni}$  heating does not cause much mixing.

Nevertheless, there are limitations in our model. The explosions take 1D KEPLER models as inputs; the convective core in the presupernovae model may produce hot spots or off-center ignitions and produce inhomogeneous distribution of  $^{56}\text{Ni}$ , which may enhance the mixing during the later radioactive heating. In addition, hydrodynamic models cannot catch the decoupling of radiation and gas in the late time, which is subject to different kinds of radiation-hydro instabilities.

The total energy budget of  $^{56}\text{Ni}$  in each model is about  $1.58-3.07 \times 10^{51}$  erg, while the explosion energy on order of  $45-55 \times 10^{51}$  erg is about twenty times larger than the decay energy. Therefore, the decay plays only a minor role in the dynamics. Nevertheless, if just half of the radioactive energy turns into the SNe light curves, say  $\sim 1 \times 10^{51}$  erg, it can easily power SLSNe by assuming a peak barometric luminosity of  $\geq 10^{44}$  erg for shining 100 days. In terms of the gas dynamics, the energy deposited from  $^{56}\text{Ni}$  decay is used to push up the gas by doing adiabatic work of  $W = PdV$ , where  $P$  is the gas pressure, and  $dV$  is the volume elements. If all the decay energy of  $1.58-3.07 \times 10^{51}$  erg is completely converted into the kinetic energy of the inner ejecta under the  $^{28}\text{Si}$  shell of  $\sim 40-50 M_{\odot}$ , the net velocity gain for this part of the star is about  $2-3 \times 10^8$  cm sec $^{-1}$ , which is consistent with the results from our simulations. The deposited energy barely pushes the inner ejecta to form a shell but cannot accelerate to the shell fast enough to form a shock that can drive fluid instabilities more efficiently.

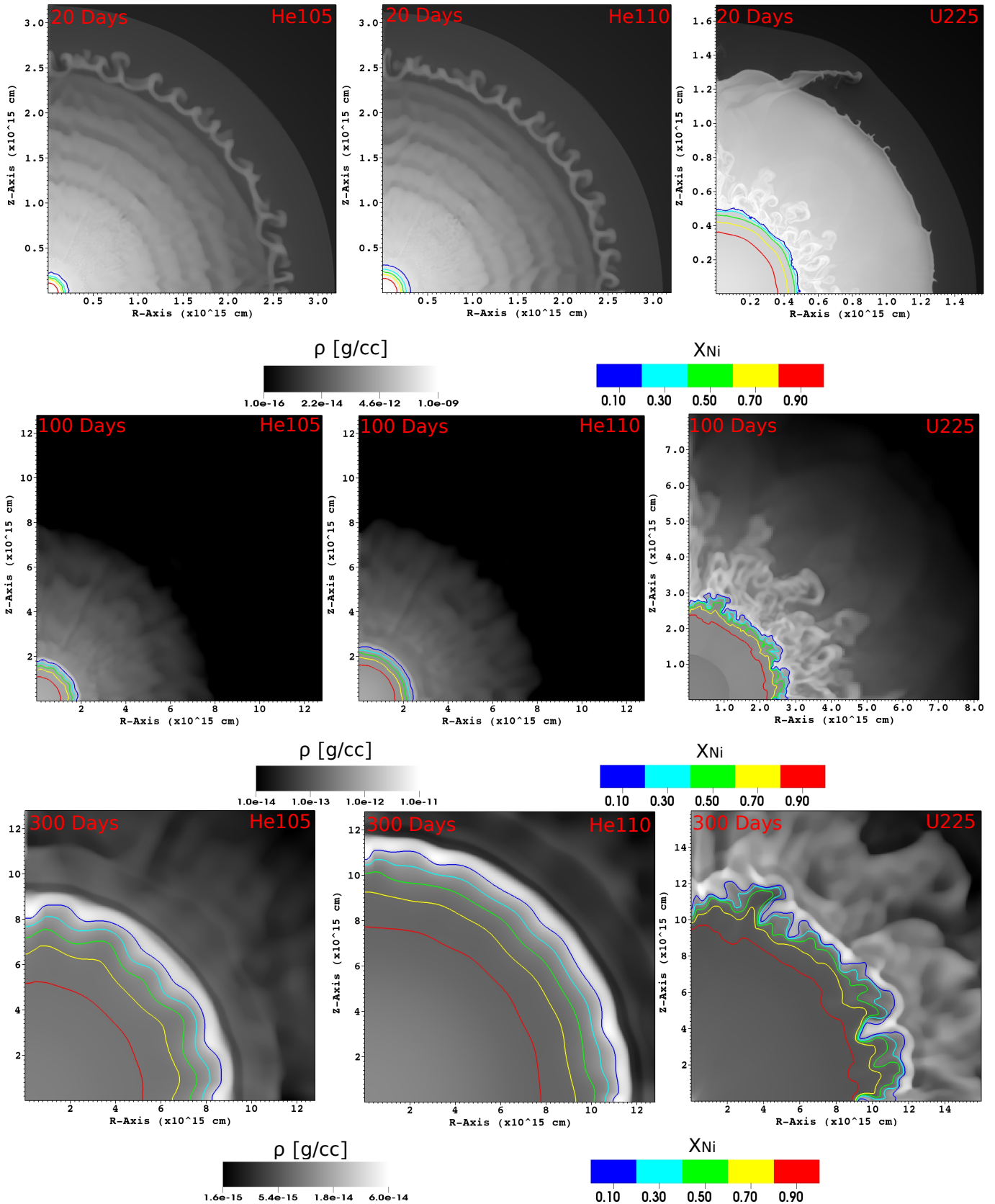


**Figure 4.** Density and  $^{56}\text{Ni}$  distribution of He105, He110, U225 at 20, 100, and 300 days. The density and  $^{56}\text{Ni}$  distribution of He105 and He110 remain spherical during the entire evolution. Visible RT instabilities appear in U225, and they start to dredge up the layer of  $^{56}\text{Ni}$  at 100 days. Each model shows a density shell located at the inner ejecta at 300 days.

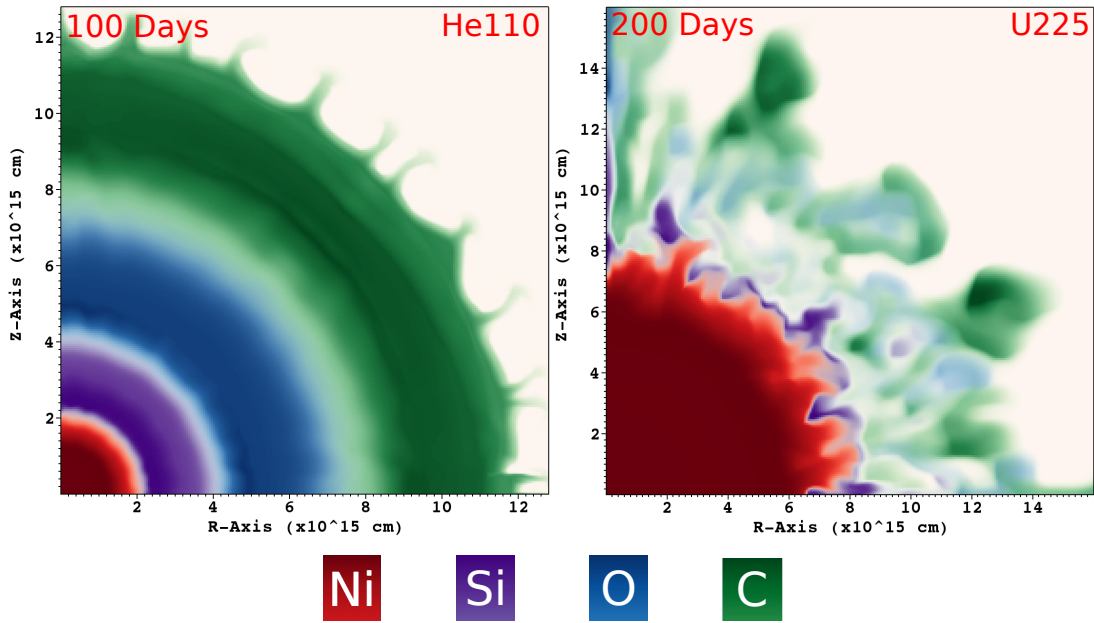


**Figure 5.** Mixing of elements. Colors represent different chemical elements in the PISNe ejecta. The elemental distribution of He110 remains shellular. However, the outer edge of the  $^{56}\text{Ni}$ -rich region in U225 has mixed with shells of  $^{28}\text{Si}$ ,  $^{16}\text{O}$ , and  $^{12}\text{C}$ .

## 5. DISCUSSIONS

Since PISNe is one of the competing models for explaining SLSNe, it is interesting to compare the fluid instabilities in the SLSNe of PISNe and those of magnetars (Blondin et al. 2001; Chevalier & Irwin 2011; Chen et al. 2016). The luminosity of SLSNe from PISNe and magnetars is powered by two distinctive engines: radioactive energy from  $^{56}\text{Ni}$  decay and the spin-down energy from a magnetar. From the results of Chen et al. (2016), the significant mixing occurs in the magnetar-powered SLSNe. So far both PISNe and magnetar can produce the light curves to fit the SLSNe well. The spectral signatures of SLSNe can be used to distinguish their engines. For SLSNe from PISNe, the decay products of  $^{56}\text{Ni}$  suggest that strong  $^{56}\text{Fe}$  lines should be visible in their nebular phases. SLSNe powered by magnetars easily show asymmetry ejecta and quick spectral evolution due to a strong mixing.

How does the stellar rotation affect the fates of PISNe? Chatzopoulos et al. (2015) suggest the stellar rotation shifts the mass of PISN progenitor stars to a lower mass window due to the homoge-

neous evolution of rotational mixing, which grows the helium core mass. If VMS are born with a rapid rotation, there is a greater probability of detecting PISNe in the local and early universes. Chen (2015) studied the impact of rotation on PISNe during the explosions phase; the results suggested that the centrifugal force from rotation can provide a resistance force to the core contraction and decrease the explosion energy and  $^{56}\text{Ni}$  production in PISNe. The overall mixing becomes weaker in the rotational models. Rotation plays a vital role in the stellar evolution of VMS and the outcomes of their PISNe. We ignore rotation in these models in this paper. The reduction of  $^{56}\text{Ni}$  production in PISNe caused by a rapid rotation suggests a weaker radioactive heating and kinematic impact on the ejecta.

VMS shine close to the Eddington luminosity. If there is a trace of metal in the envelope, the radiation easily blows the gas out and strips its envelope. The dependence of the metallicity and the mass-loss of VMS is quite unclear. Mass-loss affects the stellar evolution dramatically. Nevertheless, the Pop III ( $Z = 0$ ) and metal-poor stars ( $Z \leq 0.01Z_{\odot}$ )

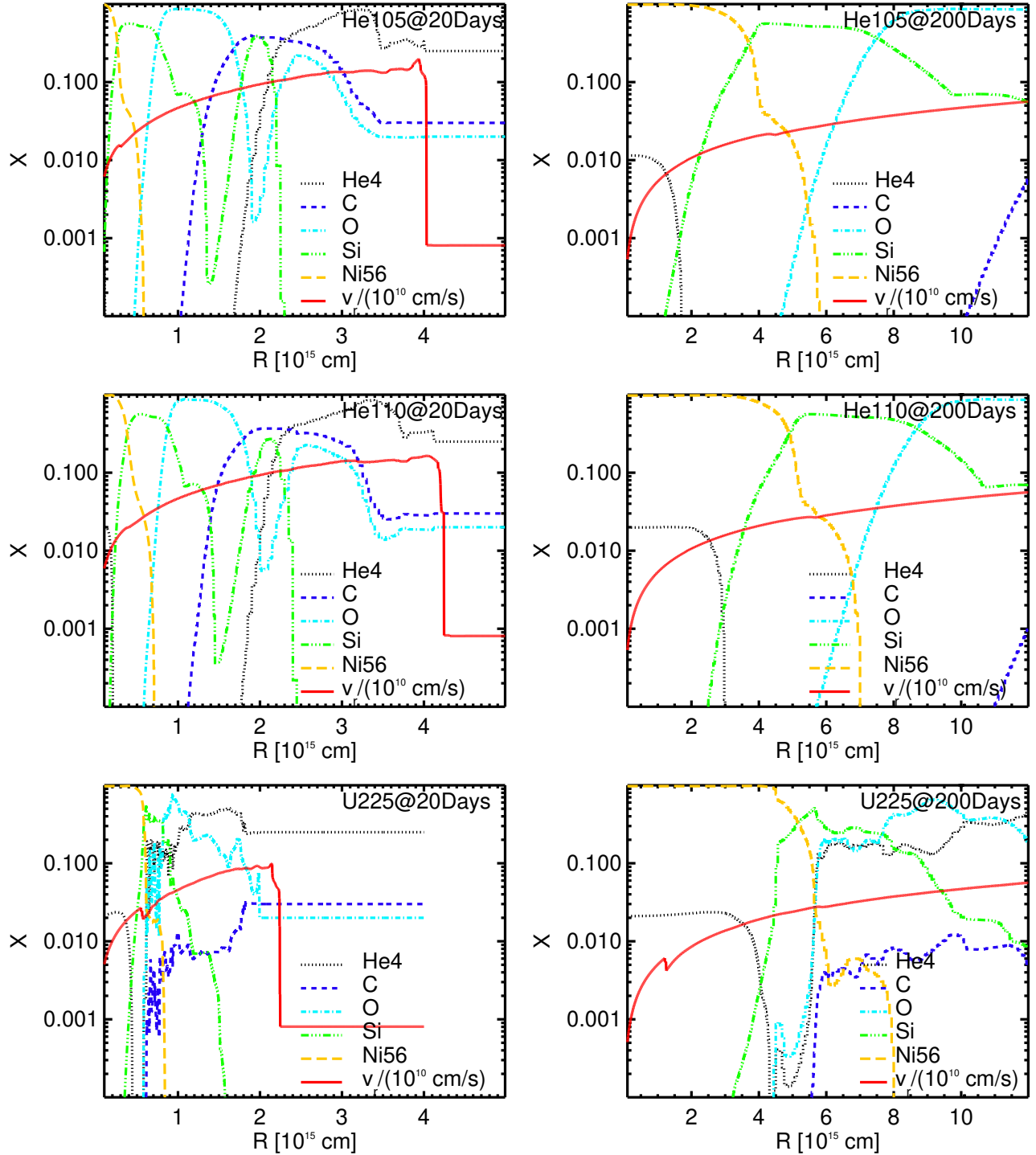


**Figure 6.** Evolution of the abundance patterns with velocities curves. The expanding ejecta stretch out the abundance patterns in the spacial coordinate. The abundance patterns of He105 and He110 stretch out with time and remain similar to the original yield of explosions. However, that of U225 has changed much. A clear kink at  $r \sim 10^{15}$  cm in velocity curve of U225 suggests a reverse shock formation.

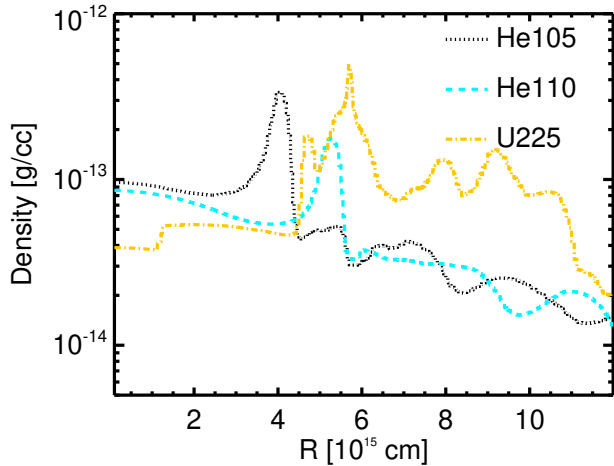


**Figure 7.** The density profile of inner ejecta. After 200 days since explosion,  $\sim 90\%$  of decay energy from  $^{56}\text{Ni} \rightarrow ^{56}\text{Co} \rightarrow ^{56}\text{Fe}$  has deposited in the SN ejecta (mostly to the inner region). Visible density shells located at  $r \sim 4 - 6 \times 10^{15}$  cm are caused by the radioactive heating. The shell in U225 is distorted due to mixing.

are promising progenitor stars of PISNe, which would be prevalent in the early universe.

Our 2D simulations show little mixing driven by the radioactive heating of  $^{56}\text{Ni}$ . What happens if we perform the same setup with 3D simulations? [Chen et al. \(2017\)](#) suggest that the 3D hydro simulation of mixing is weaker than 2D mixing because of the behavior of turbulence. The small-scale fluid instabilities in 2D are enhanced by the inverse-cascade of turbulence and produce a stronger mixing than 3D. Therefore, 2D simulations produce viable indicators of any fluid instabilities before researchers proceed with expensive 3D runs. The 2D mixing results are expected to set an upper limit for 3D mixing for the same model.

The radioactive energy of  $^{56}\text{Ni}$  decay originally emits in the form of  $\gamma$ -ray. In this study, we do not consider the  $\gamma$ -ray transfer and simply deposit it to the internal energy of gas. The assumption is validated at the optical thick regions, where photons are tightly coupled with gas. However if the gas density is getting lower at a later time or dredging up the  $^{56}\text{Ni}$  to the optical thin region, the energetic photons may start to decouple from the gas, then

the one fluid approximation breaks down. A sophisticated radiation transport of  $\gamma$ -ray with Compton scattering is required to address this issue from the first principles.

## 6. SUMMARY AND CONCLUSION

PISNe are the biggest thermonuclear explosions in the universe. Their explosion mechanisms are better understood than other stellar explosions, such as core-collapse SNe, Ia SNe, etc. The explosive oxygen and silicon burning powers the explosion and synthesizes a large amount of  $^{56}\text{Ni}$  at the same time. Tens of solar masses of  $^{56}\text{Ni}$  deposit energy of several  $10^{51}$  erg to the ejecta and radiation. However, how the radioactive energy is distributed between gas energy (internal and kinetic) and radiation remains uncertain. Previous light curves of PISNe from 1D radiation hydro models ignore the impact of radioactive energy to the dynamics of ejecta. Recent multidimensional models demonstrate the emergent fluid instabilities during PISNe explosions. We investigate the dynamic effect of  $^{56}\text{Ni}$  heating by performing high-resolution 2D simulations of PISNe and evolve the models for 300 days to complete the decay process of  $^{56}\text{Ni} \rightarrow ^{56}\text{Co} \rightarrow ^{56}\text{Fe}$ . The overall mixing from helium stars is weaker than that of red supergiant stars due to the difference in their stellar structures. All of the selected models have a  $10^{51}$  erg radioactive energy that has the capacity to power SLSNe. However, such energy is smaller compared with the explosion energy of PISNe of  $\sim 4 - 5 \times 10^{52}$  erg, which dominates the dynamics of ejecta. The resulting heating creates a shell only at the inner ejecta, which is much more distorted in the red supergiant than in the helium star. We summarize the mixing of PISNe in the different epochs of explosion:

- Presupernovae  
VMS tend to develop an extensive convective core before reaching their presupernovae. However, multidimensional stellar evolution models of VMS are unavailable

in the literature. The mixing seeded in pre-PISNe is largely unknown.

- Core contraction and explosive burning  
Chen et al. (2011, 2014) have simulated the PISNe of different progenitors from the core contraction to explosion. In their studies, they found mixing in the oxygen shell due to the RT fingers driven by the shock burning. However, its mixing time scale is short of  $\sim 10-100$  sec and its magnitude is small. This mixing is relatively weak and does not dredge up  $^{56}\text{Ni}$  to outer layers.
- Shock Propagation  
When the shock propagates through a hydrogen envelope, the shock is decelerated by its snowplowing the gas ahead of it, then a reverse shock forms. The reverse shock creates a pressure inversion to the density gradient and develops RT instabilities. In the case of the PISNe of red supergiants, their large hydrogen envelope can drive a strong reverse shock and dredge  $^{56}\text{Ni}$ -rich ejecta to the  $^{16}\text{O}$ - and  $^{12}\text{C}$ -burning shells. This mixing is strong enough to affect the PISNe spectra.
- Radioactive heating by  $^{56}\text{Ni}$  decay  
The  $^{56}\text{Ni}$  decay energy releases up to  $\sim 1.86 \times 10^{51}$  erg for  $10 M_{\odot}$  of  $^{56}\text{Ni}$  after 300 days since the explosion. Assuming that all of this energy heats up the most inner ejecta, it then pushes out the gas and creates a shell. However, our hydro simulations suggest there is minimal mixing from this shell. Since part of this energy must be used for the adiabatic expansion instead of radiation, the total amount of radiation energy from PISNe should become smaller. In comparison with the observational signatures from 1D models, our simulations suggest the peak and duration of light curves of PISNe would decrease, but the spectra remain similar to those of the previous 1D results.

Pair-instability supernovae would have been prevalent in the early universe in which the initial mass function of Population III stars is likely to have been top heavy. Given a better understanding of the physics behind PISNe, we may see that PISNe may serve as ideal targets for the next generation of telescopes, such as the *James Webb Space Telescope* (JWST), *Wide Field Infrared Survey Telescope* (WFIRST), *Thirty Meter Telescope* (TMT), *European Extremely Large Telescope* (E-ELT), and *Giant Magellan Telescope* (GMT) to probe the first stars and their supernovae. Therefore, gaining a complete understanding of the radiative process of the PISN is timely and essential. To improve the current models in this paper, we plan to use multi-dimensional radiation hydrodynamic simulations to evaluate the  $^{56}\text{Ni}$  emissions with gas dynamics by considering sophisticated  $\gamma$ -ray radiation transfer. Our future work will push the envelope of modern computational astrophysics, and it will be realized within the next few years.

We thank Alexander Heger for many useful discussions. This research is supported by an EA-COA Fellowship, and by the Ministry of Science and Technology, Taiwan, R.O.C. under Grant no. MOST 107-2112-M-001-044-MY3. KC thanks the hospitality of the Aspen Center for Physics, which is supported by NSF PHY-1066293, and the Kavli Institute for Theoretical Physics, which is supported by NSF PHY-1748958. Numerical simulations are supported by the National Energy Research Scientific Computing Center (NERSC), a U.S. Department of Energy Office of Science User Facility operated under Contract No. DE-AC02-05CH11231, the Center for Computational Astrophysics (CfCA) at National Astronomical Observatory of Japan (NAOJ), and the TIARA Cluster at the Academia Sinica Institute of Astronomy and Astrophysics (ASIAA).

## REFERENCES

- Almgren, A. S., Beckner, V. E., Bell, J. B., et al. 2010, *ApJ*, **715**, 1221
- Arnett, D., Meakin, C., & Young, P. A. 2009, *ApJ*, **690**, 1715
- Barkat, Z., Rakavy, G., & Sack, N. 1967, *Physical Review Letters*, **18**, 379
- Blondin, J. M., Chevalier, R. A., & Frierson, D. M. 2001, *ApJ*, **563**, 806
- Chatzopoulos, E., van Rossum, D. R., Craig, W. J., et al. 2015, *ApJ*, **799**, 18
- Chatzopoulos, E., & Wheeler, J. C. 2012, *ApJ*, **760**, 154
- Chen, K., Heger, A., & Almgren, A. S. 2011, *Computer Physics Communications*, **182**, 254
- Chen, K.-J. 2015, *Modern Physics Letters A*, **30**, 1530002
- Chen, K.-J., Heger, A., & Almgren, A. S. 2013, *Astronomy and Computing*, **3**, 70
- Chen, K.-J., Whalen, D. J., Wollenberg, K. M. J., Glover, S. C. O., & Klessen, R. S. 2017, *ApJ*, **844**, 111
- Chen, K.-J., Woosley, S., Heger, A., Almgren, A., & Whalen, D. J. 2014, *ApJ*, **792**, 28
- Chen, K.-J., Woosley, S. E., & Sukhbold, T. 2016, *ApJ*, **832**, 73
- Chevalier, R. A., & Irwin, C. M. 2011, *ApJL*, **729**, L6
- Colella, P., & Woodward, P. R. 1984, *Journal of Computational Physics*, **54**, 174
- Crowther, P. A., Schnurr, O., Hirschi, R., et al. 2010, *MNRAS*, **408**, 731
- Davidson, K., & Humphreys, R. M. 1997, *ARA&A*, **35**, 1
- de Souza, R. S., Ishida, E. E. O., Johnson, J. L., Whalen, D. J., & Mesinger, A. 2013, *MNRAS*, **436**, 1555
- Gilmer, M. S., Kozyreva, A., Hirschi, R., Fröhlich, C., & Yusof, N. 2017, *ApJ*, **846**, 100
- Glatzel, W., Fricke, K. J., & El Eid, M. F. 1985, *A&A*, **149**, 413
- Hartwig, T., Bromm, V., & Loeb, A. 2018, *MNRAS*, **479**, 2202
- Heger, A., & Woosley, S. E. 2002, *ApJ*, **567**, 532
- . 2010, *ApJ*, **724**, 341
- Hirano, S., Hosokawa, T., Yoshida, N., et al. 2014, *ApJ*, **781**, 60
- Hummel, J. A., Pawlik, A. H., Milosavljević, M., & Bromm, V. 2012, *ApJ*, **755**, 72
- Humphreys, R. M., & Davidson, K. 1979, *ApJ*, **232**, 409
- Kasen, D., Woosley, S. E., & Heger, A. 2011, *ApJ*, **734**, 102
- Kozyreva, A., & Blinnikov, S. 2015, *MNRAS*, **454**, 4357
- Kozyreva, A., Blinnikov, S., Langer, N., & Yoon, S.-C. 2014, *A&A*, **565**, A70
- Meakin, C. A., & Arnett, D. 2007, *ApJ*, **667**, 448
- Meiksin, A., & Whalen, D. J. 2013, *MNRAS*, **430**, 2854
- Mesler, R. A., Whalen, D. J., Smidt, J., et al. 2014, *ApJ*, **787**, 91
- Nadyozhin, D. K. 1994, *ApJS*, **92**, 527
- Ober, W. W., El Eid, M. F., & Fricke, K. J. 1983, *A&A*, **119**, 61
- Pan, T., Kasen, D., & Loeb, A. 2012, *MNRAS*, **422**, 2701
- Stringfellow, G. S., & Woosley, S. E. 1988, in *Origin and Distribution of the Elements*, ed. G. J. Mathews, 467
- Takahashi, K., Yoshida, T., & Umeda, H. 2018, *ApJ*, **857**, 111
- Timmes, F. X., & Swesty, F. D. 2000, *ApJS*, **126**, 501
- Weaver, T. A., Zimmerman, G. B., & Woosley, S. E. 1978, *ApJ*, **225**, 1021
- Whalen, D. J., Fryer, C. L., Holz, D. E., et al. 2013, *ApJL*, **762**, L6
- Whalen, D. J., Smidt, J., Heger, A., et al. 2014, *ApJ*, **797**, 9
- Woodward, P. R., Herwig, F., & Lin, P.-H. 2014, *ApJ*, **798**, 49
- Woosley, S. E., Heger, A., & Weaver, T. A. 2002, *Reviews of Modern Physics*, **74**, 1015
- Zhang, W., Howell, L., Almgren, A., Burrows, A., & Bell, J. 2011, *ApJS*, **196**, 20